EDGE ARTICLE

Check for updates

Artificial intelligence driven molecule adsorption prediction (AIMAP) applied to chirality recognition of amino acid adsorption on metals†

Zi-Xing Guo, [a] Guo-Liang Song*[a] and Zhi-Pan Liu [ID] *[abc]

Predicting the adsorption structure of molecules has long been a challenging topic given the coupled complexity of surface binding sites and molecule flexibility. Here, we develop AIMAP, an Artificial Intelligence Driven Molecule Adsorption Prediction tool, to achieve the general-purpose end-to-end prediction of molecule adsorption structures. AIMAP features efficient exploration of the global potential energy surface of the adsorption system based on global neural network (G-NN) potential, by rapidly screening qualified adsorption patterns and fine searching using stochastic surface walking (SSW) global optimization. We demonstrate the AIMAP efficiency in constructing the Cu-HCNO6 adsorption database, encompassing 1 182 351 distinct adsorption configurations of 9592 molecules on three copper surfaces. AIMAP is then utilized to identify the best adsorption structure for 18 amino acids (AAs) on achiral Cu surfaces and the chiral Cu(3,1,17)^S surface. We find that AAs chemisorb on copper surfaces in their highest deprotonated state, through both the carboxylate-amino skeleton and side groups. The chiral recognition is identified for the D-preference of Asp, Glu, and Tyr, and L-preference for His. The physical origin for the enantiospecific adsorption is thus rationalized, pointing to the critical role of the competitive adsorption between functional side groups and the carboxylate-amino skeleton at surface low-coordination sites.

1 Introduction

The molecule–surface interaction is at the heart of many branches of science. Molecular adsorption not only can modify the surface electronic/optical properties, but also may reshape the surface structures, and dictate the molecular reactivity.[1,2] The characterization of molecular adsorption, including molecule conformation, the anchoring site, and the adsorption strength, is however very challenging in experiments due to the dynamic nature of molecules on surfaces at finite temperatures. From a theoretical point of view, the molecule–surface adsorption system can be defined as a complex thermodynamic ensemble that encompasses a vast array of energetically nearly degenerate configurations (usually within a few tenths of eV), the population of which exponentially scales with varied adsorption sites, coordination atoms, and molecule conformations. As a result, the fast prediction of the molecule–surface interaction remains not feasible to date.

As a representative molecule–surface system, amino acid (AA) adsorption on metals has important applications in template synthesis,[3–6] enantiospecific adsorption,[7–11] and metal corrosion inhibition.[12–16] To date, the investigation has been limited to relatively small-sized AAs, *e.g.*, Gly, Ala, Ser[17–22] where the "brute-intuition"[23] heuristic protocol is utilized to find the adsorption configuration, *i.e.*, the local optimization with pre-guessed geometries.[19,21,24,25] Even for the simplest AA, such as Gly, there is a considerable number of likely adsorption geometries, for instance, 45 tridentate-configurations on Cu(3,1,17)^S as enumerated by Rankin *et al.*[19] For larger AAs such as Asp, and His, the structure search becomes prohibitive since multidentate adsorption configurations are coupled with the inherent flexible molecular geometry to generate a huge configuration space.

The rigorous way to find the adsorption structure would require quantum-mechanics-based[26–28] either global optimization[29,30] or long-time molecular dynamics (MD) simulations,[31–35] which is often computationally too demanding even for medium-sized molecules (*e.g.*, 10 atoms). Indeed, there are only

[a] Collaborative Innovation Center of Chemistry for Energy Material, Shanghai Key Laboratory of Molecular Catalysis and Innovative Materials, Key Laboratory of Computational Physical Science, Department of Chemistry, Fudan University, Shanghai 200433, China. E-mail: guoliangsong@fudan.edu.cn; zpliu@fudan.edu.cn

[b] Key Laboratory of Synthetic and Self-Assembly Chemistry for Organic Functional Molecules, Shanghai Institute of Organic Chemistry, Chinese Academy of Sciences, Shanghai 200032, China

[c] Shanghai Qi Zhi Institution, Shanghai 200030, China

† Electronic supplementary information (ESI) available: Theoretical methods; training and benchmark for the Cu–C–H–O–N quinary G-NN potential; insight on the Cu-HCNO6 database; structural and energetic details for AA adsorption on achiral Cu(111), Cu(100), and Cu(211) surfaces, as well as the chiral Cu(3,1,17)^S surface; the snapshots of the enantio-specific adsorption of Glu and Tyr on the Cu(3,1,17)^S surface. See DOI: https://doi.org/10.1039/d4sc02304h

a few reports, less than 30 systems (a molecule on a surface), in the literature.[23,36] For example, Peterson searched the global minima (GM) of 17 $C_xH_yO_z$ molecules on the Cu(211) surface by using DFT calculations and the constrained minima hopping (CMH) global optimization algorithm.[23] The recent effort is thus directed to the database construction of adsorption structures using density functional theory (DFT) calculations without seeking the most stable configuration, such as the OC20 data-base (Open Catalyst 2020) project that contains a total of 1.28 million DFT results of simple molecule adsorption on a wide swath of materials (11 451 materials in total, 95% are binary or ternary, with up to 55 unique elements).[29] The molecule types in the OC20 dataset are limited to only 82 small-sized adsorbates, mainly C1/C2 compounds and N/O-containing intermediates, less than 7.0×10^{-5} percent of the vast molecular space recorded in PubChem (117 million unique chemical structures).[37] The lack of molecule generality is understandable since the database generation is both labor and computation intensive where the precursors for each adsorbate have to be generated by enumerating many likely adsorption sites, followed by DFT-level local geometry optimization to identify favorable adsorption sites and energetics. In the OC20 generation, to reduce the computational costs, only *ca.* 0.07% of the possible precursors are selected randomly, each with one local minimum (LM).

Recent advances in machine learning (ML) based algorithms provide a new avenue for theoretical simulations to fast explore the PES of complex systems.[38,39] For instance, our group showed in recent years that the stochastic surface walking (SSW) global optimization based on the global neural network (G-NN) potential (SSW-NN) can explore global PES unbiasedly *via* the smooth structure perturbation with an accuracy comparable to DFT calculations.[40–42] The SSW-NN has been utilized to explore the molecule reaction network on metal surfaces, which yields not only the GM of molecular adsorption structures but also the reaction transition state (TS).[43–48]

Here we introduce AIMAP, an artificial intelligence (AI)-based end-to-end tool for predicting molecular adsorption energetics and configurations. We demonstrate the power of AIMAP by establishing the first molecule-Cu database, which encompasses 9592 distinct adsorbates of up to 6 skeleton atoms (*i.e.*, C, N, and O) on Cu(111), Cu(100), and Cu(211) surfaces with all results released online (**http://laspmol.lasphub.com/laspmol_surf.asp**). With this new tool, we explore the adsorption of 18 AAs on three achiral copper surfaces and also predict the enantioselectivity of AAs on intrinsic chiral $Cu(3,1,17)^S$. Our results pave the way for fully automated computational prediction of molecule adsorption and surface reaction energetics *via* AI-based methods.

2 AIMAP method and Cu-HCNO6 database

2.1 AIMAP method

Our AIMAP method is developed to determine, in an automated way, energetically-favored molecule configurations on surfaces with simple inputs, *e.g.*, starting from the chemical name of the

adsorbate and surface Miller index. The hierarchy workflow of the method is depicted in Fig. 1, which contains four stages, namely, (i) Molecular Conformation Generation (**I-MCG**); (ii) Adsorption Precursor Enumeration (**II-APE**); (iii) Neural Network potential based precursor Screening (**III-NNS**); (iv) SSW-NN-based Structural Space Exploration (**IV-SSE**). Unlike previous methods, AIMAP considers all likely chemisorption connectivity in generating surface precursors and incorporates a neural network potential to speed up the precursor screening (at the stage **III-NNS**), and employs the SSW-NN method for the GM global exploration (at the stage **IV-SSE**). More details about the G-NN potential and SSW-NN method can be found in ESI Section 1.† The four stages are outlined in the following with the adsorption of the non-deprotonated glycine on the Cu(211) surface as the example.

2.1.1 I-MCG. This initial stage is to read the chemical name of molecules (*e.g.*, SIMILES name, skeletal formula) and convert it into a series of 3-D coordinates for the molecule. We follow the standard approach to generate a 3-D structure using the Open Babel package[49] and to enumerate the gas-phase conformation using the x-TB package.[50,51] The G-NN potential is utilized to further refine the geometry and provide the gas phase energetics of all conformers. For glycine in the gas phase, this structural ensemble contains 7 conformers.

2.1.2 II-APE. This stage involves the exhaustive enumeration of surface precursors based on the 3-D structures of adsorbates. The chemisorption model is built *via* three steps (i) selecting adsorption-active sites of the adsorbate, preferentially O, N, unsaturated C, and acidic H; (ii) placing the molecule on the surface and rotating the coordination bonds to generate possible precursors; (iii) removing duplicate structures with identical adsorption modes. On the flat surfaces (*e.g.*, Cu(111) and Cu(100) facets), all copper atoms are considered equivalently, whereas on stepped surfaces, only defective copper atoms (*e.g.*, step edge on the Cu(211) surface) are considered as the molecule adsorption sites. The adsorbates are configured on the top of adsorption sites, whereas other high-symmetrical sites such as fcc/hcp hollow and bridge sites are not explicitly considered. The further exploration of different adsorption sites will be complemented by the downstream SSW global exploration at stage **IV-SSW**. Duplicate structures produced by brute enumerations are ruled out by considering the root-mean-square deviation (RMSD) between the adsorbate's Cartesian coordinates.

Fig. 1 illustrates one of the typical arrangements of glycine on the Cu(211) surface, which incorporates three atoms, *i.e.*, carboxyl oxygen, α-hydrogen, and amino nitrogen. The adsorbate is arranged 2.0 Å above the surface, with the oxygen atom located at the top site on the step edge. Each 60° rotation through the Cu–O axis produces one brute precursor. A total number of 263 structures are enumerated with other arrangements and rotations. A 1.0 Å cutoff is set to rule out duplicate structures and finally produce 57 distinct adsorption conformations.

2.1.3 III-NNS. In this stage, the G-NN potential is employed to locally optimize the surface precursors provided by stage **II-APE**. As a result, high-energy structures are screened out. The
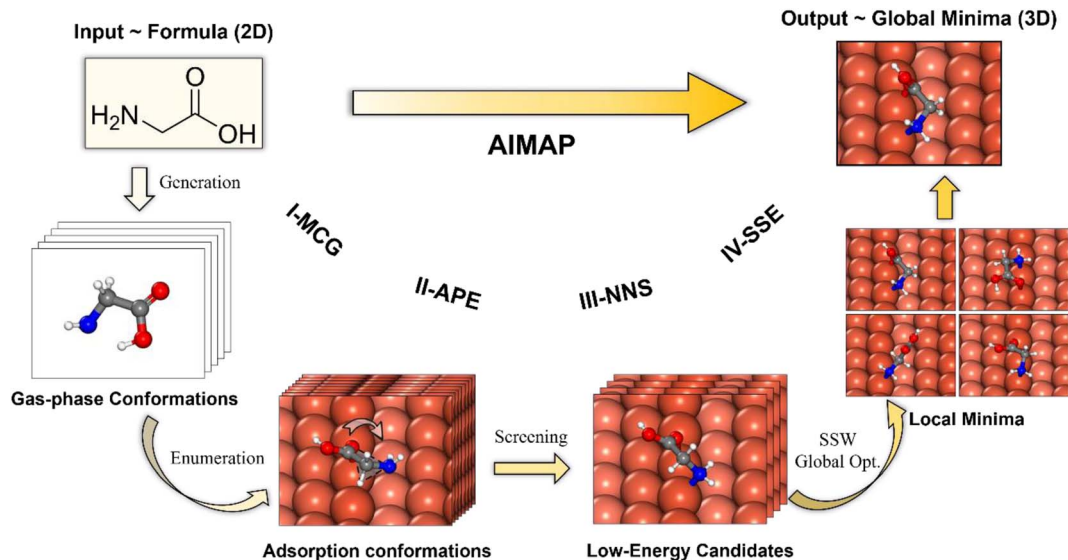
Fig. 1 Workflow of the AIMAP algorithm. AIMAP features an automatic end-to-end procedure to obtain the most stable adsorption structure (*e.g.*, GM) using the 2D molecule information as input. It contains four stages: (i) molecule gas phase conformation generation (**I-MCG**); (ii) adsorption precursor enumeration (**II-APE**); (iii) fast screening based on G-NN potential local optimization (**III-NNS**); (iv) SSW-NN-based global exploration of low energy adsorption candidates (**IV-SSE**). The non-deprotonated glycine on the Cu(211) surface is utilized to exemplify the four stages. Colors in this figure: white balls are H; grey balls are C; blue balls are N; red balls are O; coral balls are Cu (with those closer to the step-edge of Cu(211) exhibiting a higher color intensity).

remaining low-energy structures are kept as candidates in the subsequent stage **IV-SSW**, the number of which is a system-dependent parameter (N_{IS}), typically below 30 structures.

Fig. 1 illustrates the selected precursors for the glycine/Cu(211) system after the screening. A total number of 10 structures are identified ($N_{IS} = 10$). The most favorable precursor can directly produce multi-dentation configurations with a single-step optimization.

2.1.4 IV-SSE. In this stage, the SSW-NN method is utilized to explore the adsorption configuration space, starting from candidates obtained in stage **III-NNS**. With the cascade screening of molecule configurations in previous steps, we found that a limited number of SSW steps (N_{SSW}, *e.g.*, <30 SSW steps) are typically enough to identify the best adsorption geometry, namely, the GM structure. In this work, the "GM" refers to the most stable structured identified for a specific state of the molecule, *e.g.*, the non-deprotonated state, the mono-deprotonated state, and so on.

Fig. 1 illustrates the GM and top 4 LM for the glycine/Cu(211) system, which are obtained by 5 steps of SSW global search ($N_{SSW} = 5$). The GM features the μ_2 configuration (μ_n(-X): 'n' signifies the number of adsorbed atoms with X labeling their elements) with O and N atoms binding on the step edge.

In Table 1, we list the statistics for AIMAP in identifying the adsorption GM for methanol, non-deprotonated glycine, and mono-deprotonated asparagine (aspartate) on Cu(211) surfaces. It can be seen that with the increase of molecular complexity from methanol to aspartate, the parameters N_{IS} (**III-NNS**) and N_{SSW} (**IV-SSE**) need to be increased to identify the GM. The computation time in the fully automated AIMAP search also increases from 67 s to 701 s on a typical 28 CPU

workstation, which is understandable as both glycine and aspartate prefer multidentate adsorption, *e.g.*, μ_2, μ_5, which was typically a formidable task[52] in the adsorption structure search. It should be emphasized that not only the GM is identified, but a set of LM with relatively low energy are also obtained from AIMAP, which is very useful for understanding the adsorption behavior of molecules and is exemplified in ESI Fig. S2.† In the following sections, we set N_{IS} (**III-NNS**) = N_{SSW} (**IV-SSE**) = 15 for generating the Cu-HCNO6 database. For careful investigation of adsorption structures of AAs, the

Table 1 Accounts on the typical results and costs of AIMAP in finding molecule adsorption structures.[a] Listed data include the name of exemplified molecules, molecule size (C/N/O only), the number of candidate structures for global optimization (N_{IS}), the number of SSW searching steps (N_{SSW}), the number of LM produced by local optimization (N_{LM}), the number of distinctive LM (N_{DLM}), the description of adsorption configurations (Conf.), and the time consumption of the whole procedure (t)

Molecule name	Methanol	Glycine	Aspartate
Molecule size	2	5	9
N_{IS}	3	10	15
N_{SSW}	3	5	15
N_{LM}	9	50	225
N_{DLM}[b]	3 (2)[c]	11 (2)[c]	34 (3)[c]
Conf.	μ_1(O)	μ_2(N,O)	μ_5(4O,N)
t[d]/s	67	274	701

[a] GM identified by AIMAP is further confirmed by long SSW global optimization (>2000 steps). [b] Distinguished by root mean square deviation (RMSD) of Cartesian coordinates with the periodicity and symmetry considered. [c] Data in parentheses is the number of LM within +0.20 eV above the GM. [d] Measured on a single workstation computer: Xeon E5-2695 V3, 3.3 GHz, 2 packages, 28 cores.

parameters are raised to $N_{IS} = N_{SSW} = 30$ on achiral surfaces and are further expanded on the more complex chiral Cu(3,1,17)^S surface (*e.g.*, $N_{IS} = N_{SSW} = 45$ for asparagine).

2.2 Cu-HCNO6 database

The power of the AIMAP method is then proved by constructing a large database named Cu-HCNO6, which contains 1 182 351 distinct adsorption structures on copper surfaces. Fig. 2a summarizes the content and key features of the Cu-HCNO6 database: three typical Cu surfaces are considered, including planar Cu(111) and Cu(100), and stepped Cu(211); 9592 distinct adsorbates are included, encompassing nearly all neutral species composed of up to six C/N/O (non-H) heavy atoms in the PubChem database, where 76.2% of them possess one or more double or triple bonds (unsaturated C, *e.g.*, $CH_2 = CH_2$), and

75.7% contain at least two N/O atoms. Detailed composition analysis is provided in ESI Section 4.†

Not only the GM but also low-energy LM obtained from AIMAP are included in the Cu-HCNO6 database, which are screened out of 5 301 277 local relaxations in **IV-SSE**. Using these adsorption structures, the adsorption energy (E_{ads}) of the molecule can thus be predicted and stored in the database. Since all the energetics in the database are based on G-NN calculations, we have benchmarked the precision of adsorption energy with DFT results. On 10 000 randomly selected adsorption structures, the RMSD of adsorption energy from G-NN results and DFT results is 0.19 eV per structure (see ESI Section 5†).

Because of the huge content of the Cu-HCNO6 database, in the following, we provide a database profile by focusing on selected molecules. We choose 311 different molecules, 14 types
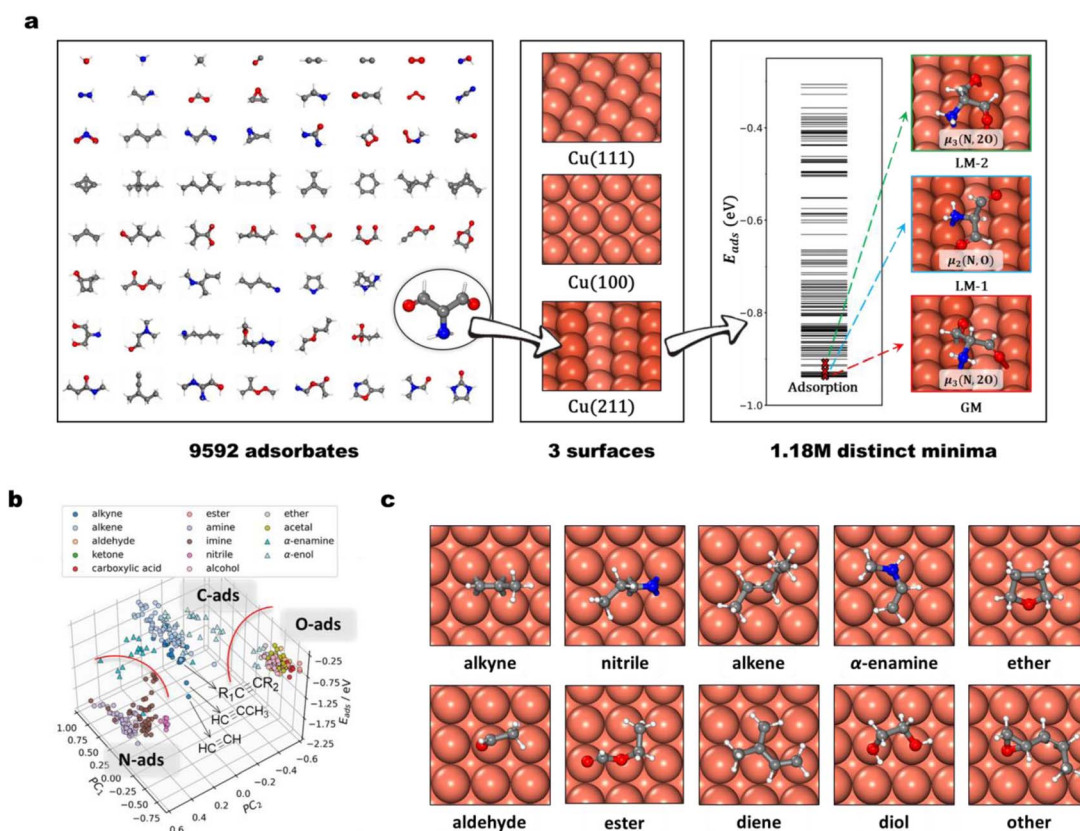

Fig. 2 Cu-HCNO6 database. (a) Database contents. The figure exemplifies 61 adsorbates out of 9592 molecules with up to six C/N/O skeleton atoms in the database. Three distinctive copper surfaces, namely Cu(111), Cu(100), and Cu(211), are included. For each adsorbate–surface combination, both GM and distinctive LM are generated automatically *via* AIMAP. Utilizing these adsorption structures, the adsorption energy (E_{ads}) of the molecule is predicted and stored in the database. (b) Scatter diagram between energetic properties (E_{ads}, *z*-axis) and geometrical features (PC$_1$, *x*-axis; PC$_2$, *y*-axis). The PC$_1$ and PC$_2$ are the top 2 highest weighted components from Principal Component Analysis (PCA) on 450 dimensions of basis consisting of power-type symmetry descriptors (PTSD) used in G-NN potential. In plotting the diagram, 311 adsorption structures on the Cu(100) surface are utilized. The structures are colored in 14 types: alkyne, alkene, aldehyde, ketone, carboxylic acid, ester, amine, imine, nitrile, alcohol, ether, acetal, α-enamine, and α-enol. These points aggregate into clusters and can be divided (by red line) into three broad regions along the *x/y*-axis, featuring N, O, and unsaturated C atoms in functional groups. Three alkynes with different alkyl substitutes are marked by black arrows to illustrate the adsorption energy difference within the same cluster. (c). Typical adsorption structures on the Cu(100) surface. Each structure is labeled by the molecule type, including seven types of mono-functional molecules (alkene, alkyne, nitrile, α-enamine, ether, aldehyde, and ester) as well as three types of multi-functional molecules (diene, diol, other). Colors in (a) and (c): white balls/sticks are H; grey balls are C; blue balls are N; red balls are O; coral balls are Cu (with those closer to the step-edge of Cu(211) exhibiting a higher color intensity).

in total, from the database, distinct in the functional group feature, including alkyne, alkene, aldehyde, ketone, carboxylic acid, ester, amine, imine, nitrile, alcohol, ether, acetal, α-enamine, and α-enol. Taking these molecules on the Cu(100) surface as an example, we analyze their adsorption geometry features by using Principal Component Analysis (PCA). 450 power-type symmetry descriptors (PTSD) used in G-NN potential are utilized as the component for constructing the PCA basis, from which the top 2 highest weight components are generated (PC1, PC2) that provide the main geometric feature. Fig. 2b plots the scatter diagram between the E_{ads} energetic and PC main geometrical features, which shows an obvious clustering of the data points in the $E_{ads} \sim PC1 \sim PC2$ plot molecules with similar functional groups that tend to behave similarly.

Specifically, the adsorption geometry can be divided into three broad regions along the x/y-axis, featuring N, O, and unsaturated C atoms in their functional groups. For those with two more functional groups, for example, α-enamine and α-enol, they also appear as separate clusters, indicating the participation of multiple functional groups in adsorption (*e.g.*, both unsaturated C and N/O atoms involved in bonding with the surface). Within the same type of functional group, the adsorption energy varies in a range of typically a few tenths of eV, due to the different alkyl fragments attached to the functional group (*e.g.*, acetylene, propyne, and other alkynes, as exemplified in Fig. 2b).

We further examine carefully the adsorption structures out of the 311 molecules on the Cu(100) surface. As illustrated in Fig. 2c, we found that alkyne, alkene, nitrile, α-enamine, and α-enol adsorb strongly with their unsaturated C (N) atoms, and the molecule adopts the flat-lying geometry. On Cu(100) each triple-bonded C/N atom is located typically at one bridge site, as alkyne and in nitrile, forming a tetrahedron binding geometry (μ_2, Fig. 2c alkyne, nitrile); the double-bonded C atoms can adopt the top–top site geometry (μ_2, Fig. 2c alkene) or the top–bridge–top site (μ_3 Fig. 2c α-enamine). For N/O-containing molecules, the N/O end also prefers to bond with Cu, where the O and N atoms are typically located at the top site on Cu(100) (Fig. 2c ether, aldehyde). For molecules with multiple adsorption linker atoms (*i.e.*, O, N and unsaturated C), they can have the multidentate adsorption geometry, where by rotating the flexible single-bond of the molecule, each linker atom could achieve monodentate adsorption. For example, both two oxygen atoms bind on the top sites in ester adsorption (Fig. 2c ester). This rule applies to multiple functional group molecules, such as glycol (Fig. 2c, diol), *cis*-pentadiene (Fig. 2c, diene), and 4,5-epoxy-2-pentene (Fig. 2c, other). These molecules often form ring structures with surface Cu atoms, which further stabilize the adsorption geometry (*e.g.*, six-membered ring Cu–O–C–C–O–Cu in glycol).

It should be noted that the above analysis takes only 3.4% of adsorbates in the Cu-HCNO6 database, and on a single Cu(100) surface. For a broader range of molecule adsorption on varied surfaces, we refer to the database **http://laspmol.lasphub.com/laspmol_surf.asp** for any specific research.

3 Amino acid adsorption on Cu surfaces

Not limited to relatively small molecules involved in the Cu-HCNO6 database, we go further to predict the AA adsorption structure on Cu, which is of great significance in many applications.[3–16] Except for cysteine and methionine with the sulfur atom (not supported by the Cu–C–H–O–N G-NN potential), adsorption of all AAs (18 molecules) on the three achiral Cu surfaces (Cu(111), Cu(100) and Cu(211)) and one chiral Cu surface (Cu(3,1,17)[S]), including their neutral, anionic, and di-anionic forms, in total 43 distinct adsorbates, is investigated and their adsorption free energies under ambient conditions are evaluated to compare the relative stability. DFT calculations are further utilized to fully optimize the low-energy structures obtained from AIMAP (see ESI Section 2†). All DFT data (using PBE-D3 exchange–correlation functional) can be found in ESI Sections 6 and 7.†

To align to the same deprotonation level of adsorbates the adsorption free energy (G_{ads}) is calculated using eqn (1),

$$G_{ads} = G_{sys} + \frac{n}{2}\mu_{H_2}(T,p) - G_{surf} - G_{AA} \qquad (1)$$

where n denotes the deprotonation level; G_{sys}, G_{surf}, and G_{AA} denote the DFT total energy with zero-point energy (ZPE) correction of the (deprotonated) AA–surface adsorption system, bare surface, and isolated AA, respectively. The chemical potential μ of H_2 is given by eqn (2) as

$$\mu_{H_2}(T,p) = H_{H_2} + \Delta H_{H_2}(0 \to T, p^0) - TS_{H_2}(T, p^0) + RT \ln\left(\frac{p}{p^0}\right) \qquad (2)$$

where the values for the enthalpy change, ΔH, and entropy, S, were taken from experimental data;[53] and $p^0 = 1$ atm, $T = 298.15$ K, and $p = 10^{-10}$ mbar.

3.1 Adsorption on achiral surfaces

We only focus on L-AAs in this part, given that the adsorption structure of D/L-AAs is equivalent on achiral surfaces. As listed in Table 2, for the best adsorption structure and energetics in the GM, we find that all AAs undergo deprotonation upon adsorption on all three achiral surfaces (also see ESI Table S6†). They all achieve the multi-dentate adsorption geometry, at least tri-dentate, relating two O in the carboxylate group and N in the amino group. Among them, anion species are favored for 13 types of AAs, including Gly, Ala, Val, Leu, Ile, Pro, Phe, Trp, Gln, Asn, Lys, Arg, and His; and the di-anionic form is preferred for Ser, Thr, Tyr, Glu, and Asp where the hydroxyl or carboxyl groups in the side chains also undergo deprotonation on adsorption.

The adsorption energy is generally large, greater than 1.4 eV, where the lower coordinated surface provides higher adsorption energy in general, *i.e.*, G_{ads} follows Cu(111) < Cu(100) < Cu(211), with average value as −2.11 eV, −2.61 eV, and −2.80 eV, respectively. It is interesting to note that the van der Waals (vdW) contribution from D3 correction contributes 66.5% on

Table 2 Adsorption energy and configurations of 18 types of AAs on three Cu surfaces. Listed data include the classes of AA side chains (alkyl, aryl, and other N/O containing functional), the molecule name, the deprotonate number of the most energetically favourable adsorption species, and the adsorption free energy (G_{ads}, obtained by eqn (1)) and adsorption configuration (Conf.) on three achiral surfaces (Cu(111), Cu(100), and Cu(211))

Class	Molecule name	Deprotonation number	Cu(111)		Cu(100)		Cu(211)	
			G_{ads}	Conf.	G_{ads}	Conf.	G_{ads}	Conf.
Alkyl	Gly	1	−1.49	μ_3(2O,N)	−1.88	μ_3(2O,N)	−2.06	μ_3(2O,N)
	Ala	1	−1.62		−2.03		−2.20	
	Pro	1	−1.73		−2.06		−2.23	
	Val	1	−1.70		−2.29		−2.29	
	Leu	1	−1.83		−2.26		−2.35	
	Ile	1	−1.89		−2.29		−2.35	
Aryl	Phe	1	−2.05	μ_3(2O,N)	−2.45	μ_3(2O,N)	−2.65	μ_3(O,N,Ar)
	Trp	1	−2.49	μ_3(2O,N)	−2.72	μ_3(2O,N)	−3.20	μ_3(O,N,Ar)
	Tyr	2	−2.48	μ_4(2O,N,Ar)	−3.33	μ_3(2O,Ar)	−3.56	μ_4(2O,N,Ar)
Other N/O containing functional	Ser	2	−2.18	μ_4(3O,N)	−2.54	μ_4(3O,N)	−2.68	μ_4(3O,N)
	Thr	2	−2.32	μ_4(3O,N)	−2.67	μ_4(3O,N)	−2.77	μ_4(3O,N)
	Gln	1	−2.36	μ_3(2O,N)	−2.89	μ_4(3O,N)	−3.08	μ_4(3O,N)
	Asn	1	−1.85	μ_3(2O,N)	−2.34	μ_4(3O,N)	−2.49	μ_4(3O,N)
	Glu	2	−2.59	μ_5(4O,N)	−3.17	μ_5(4O,N)	−3.65	μ_5(4O,N)
	Asp	2	−2.30	μ_5(4O,N)	−2.86	μ_5(4O,N)	−3.11	μ_5(4O,N)
	Lys	1	−2.63	μ_4(2O,2N)	−3.39	μ_4(2O,2N)	−3.36	μ_4(2O,2N)
	Arg	1	−2.25	μ_4(2O,2N)	−2.90	μ_4(2O,2N)	−3.17	μ_3(2O,N)
	His	1	−2.26	μ_4(2O,2N)	−2.84	μ_3(2O,N)	−3.20	μ_4(2O,2N)

average to G_{ads} in Cu(111), 46.0% in Cu(100) and 44.5% in Cu(211), suggesting the significant contribution of vdW interactions for the large molecule adsorption on metals.

In the following, we elaborate on the adsorption results of 18 AAs, which can be divided broadly into three classes according to their side chains, alkyl, aryl, and N/O containing functional groups.

3.1.1 Class I alkyl side chain. These AAs possess alkyl side groups, including Gly, Ala, Val, Leu, Ile, and Pro. The average G_{ads} is lower than the other two classes, being −1.71 eV, −2.14 eV, and −2.25 eV on Cu(111), Cu(100), and Cu(211) surfaces respectively. All these AAs bind to copper surfaces through the carboxylate-amino skeleton only, featuring μ_3(2O,N) configurations on all surfaces. The main difference between these AAs is the size of alkyl chains and the adsorption strength ranks as Gly < Ala < Val < Pro < Leu ≈ Ile, following the volume of side chains (see ESI Fig. S6†). Their adsorption structure can be represented by that of Ala, as described below.

3.1.2 Ala. Fig. 3 shows that on Cu(111) and Cu(100) Ala utilizes one nitrogen atom and two oxygen atoms to bind on the top site of copper atoms, with Cu–O bond lengths of 2.07 Å, 2.18 Å, and 2.06 Å, 2.06 Å, respectively. The Cu–N bond lengths are 2.15 Å on the Cu(111) surface and 2.13 Å on the Cu(100) surface. On the stepped Cu(211) surface, the two oxygens of the carboxylate group bind to the step edge (Cu–O length, 1.97 Å, 2.02 Å), and the nitrogen of the amino group attaches to the top site of the {111} microfacet of the lower terrace (Cu–N bond length 2.16 Å).

3.1.3 Class II aryl side chain. These AAs feature aryl side-chain groups, including Phe, Tyr, and Trp. The average G_{ads} is −2.34 eV, −2.83 eV, and −3.14 eV on the three surfaces, being much larger than those of Class I AAs. The increase in G_{ads} can

be attributed to the vdW interaction between the benzene ring and Cu surfaces as reflected by the simultaneous augmentation of D3 correlation energy (see ESI Fig. S6†). A similar μ_3(2O,N) tridentated adsorption structure is adopted on two flat surfaces, while the aryl ring may also participate in bonding with the contiguous step-edge on Cu(211) (see Fig. 3). In this Class, Tyr undergoes further deprotonation on the phenolic hydroxyl group, possessing an additional binding with this O atom (e.g., μ_3(2O,Ar)) configuration for Tyr-Cu(100). Phe is selected as the representative structure to illustrate the adsorption geometry below.

3.1.4 Phe. Fig. 3 shows the typical μ_3 adsorption configurations on Cu(111) and Cu(100) where the N/O atoms adsorb on the Cu top site. The tilting angle between the phenyl ring and Cu(111) surface is 45.6° and that on the Cu(100) surface is 84.8°, nearly perpendicular. In Phe/Cu(211), it forms a μ_3(O,N,Ar) adsorption geometry. The carboxylate-amino skeleton adopts a bi-dentate configuration with a step-edge with the bond lengths of Cu–N 2.14 Å and Cu–O 1.93 Å. The benzene ring lies nearly parallel (2.2° tilting angle) with the surface with the distance being 2.32 Å between the benzene ring and the next step-edge.

3.1.5 Class III other N/O-containing side chain. These AAs feature N/O-containing functional groups in side-chains, such as hydroxyl, carboxyl, amine, and amide. 9 types of AAs, i.e., Ser, Thr, Gln, Asn, Glu, Asp, Gln, Lys, Arg, and His belong to this class. The average G_{ads} is −2.30 eV, −2.85 eV and −3.06 eV on the three surfaces, being close to Class II AAs. The functional side chains contribute additionally to the adsorption, leading to a higher dentation number. Ser and Asp are utilized as the examples to elaborate the adsorption configurations in the following.
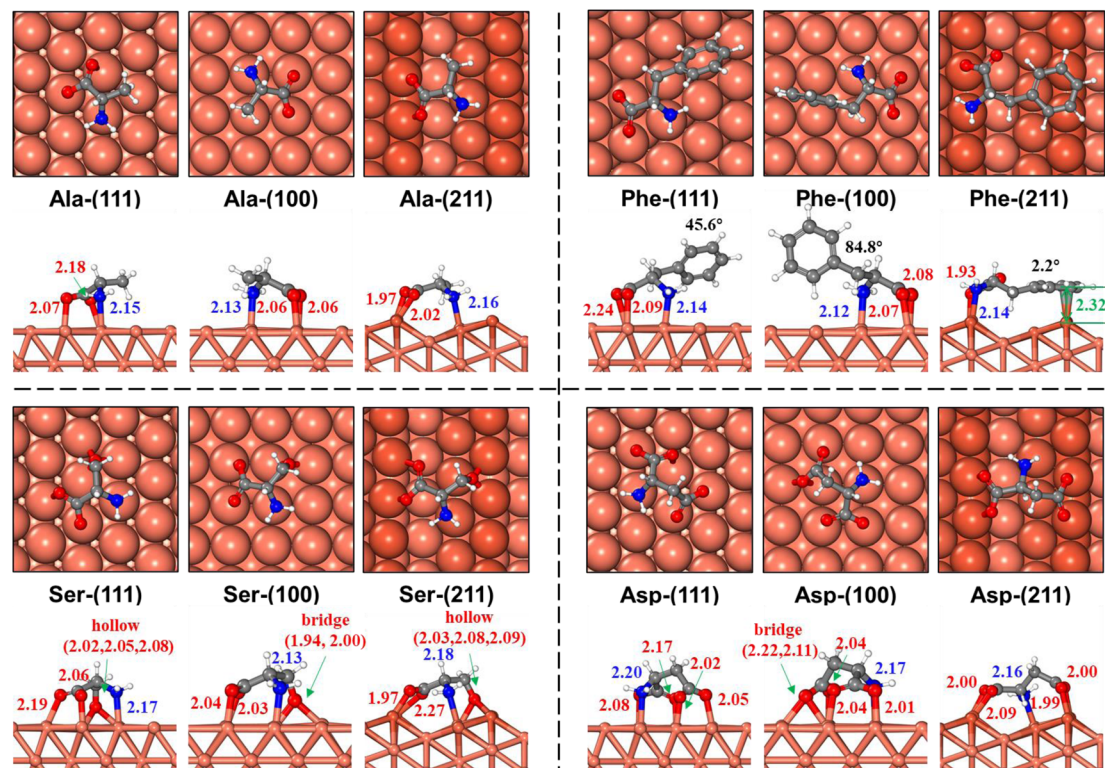
Fig. 3 Adsorption structures of four representative AAs (Ala, Phe, Ser, and Asp) on Cu(111), Cu(100), and Cu(211) surfaces. Both the top-down (ball model) and side (ball-stick model) views are provided. Important bond lengths (Angstrom) are marked: red numbers denoting Cu−O bonds, blue ones denoting the Cu−N bonds, and black ones denoting the tilting angle between the phenyl ring and surface; green denoting the distance between the phenyl ring and the Cu(211) step. Colors in this figure: white balls are H; grey balls are C; blue balls are N; red balls are O; coral balls are Cu (with those closer to the step-edge of Cu(211) exhibiting a higher color intensity).

3.1.6 Ser. Fig. 3 depicts the $\mu_4(3O,N)$ configuration of Ser adsorption on the three surfaces, involving an extra adsorption site through the deprotonated hydroxyl group. On all surfaces, the carboxylate-amino skeleton adopts the $\mu_3(2O,N)$ configuration and binds on the same site as it is in Ala. For the hydroxyl group, on Cu(111) and (211) surfaces, the deprotonated hydroxyl adsorbs on the hollow site, with three Cu−O bonds being 2.02–2.09 Å. On Cu(100), the hydroxyl oxygen atom is located at the bridge site, with 1.94 Å and 2.00 Å for Cu−O distances.

3.1.7 Asp. Fig. 3 depicts the $\mu_5(4O,N)$ configuration of Asp adsorption on the three surfaces, where $\mu_3(2O,N)$ is from the carboxylate-amino skeleton and $\mu_2(2O)$ from two carboxylate oxygen atoms in the side-chain. The binding of the carboxylate-amino skeleton is also similar to that in Ala. For the carboxylate group in the side-chain, the two O atoms bond with two Cu atoms on Cu(111) (Cu−O bond lengths of 2.02 Å and 2.05 Å) and three Cu atoms on Cu(100), one bridge site (Cu−O distance, 2.11 Å, 2.22 Å) and one top site (Cu−O distance, 2.04 Å). On Cu(211), the adsorption takes two adjacent step edges, where four oxygen atoms in Asp bind the step edge (Cu−O distance, 1.99 Å, 2.00 Å, 2.00 Å, 2.09 Å), and the nitrogen atom bonds on the {111} microfacet (Cu−N distance, 2.16 Å).

It is interesting to compare our theoretical results with experimental observations. First, the deprotonation state of AA adsorption has been observed in many experiments (above 300 K), including Gly/Cu(100), Gly/Cu(110), Ala/Cu(110), Ser/Cu(110), Asp/Cu(110), and Pro/Cu(111) systems.[17,54–62] For example, Dutta et al. found that the α-carboxyl group undergoes deprotonation in the Pro/Cu(111) system through C 1s X-ray photoelectron spectroscopy (XPS) measurements[61] and the deprotonation of side-chain groups is also observed by XPS measurements in other AAs (e.g., hydroxyl in Ser and carboxyl in Asp).[60,63] This is consistent with our results that the highest deprotonation form is preferred for all AAs on copper surfaces. Second, the multi-dentate adsorption geometry of AAs has also been deduced from experiments. By using PhD and LEED, Williams et al. observed a pair of equidistance oxygen atoms and N lone-pair interaction in the low-coverage Ala/Cu(110) system,[54] which suggests a μ_3 configuration. Eralp et al. observed a low binding-energy shoulder (530.8 eV) of O 1s XPS in the Ser/Cu(531) system, which suggests that the adsorption involves hydroxyl oxygen and thus the μ_4 configuration is proposed.[21]

3.2 Adsorption on the chiral surface

The chirality recognition via the molecule–surface interaction is an important topic in chemistry. By switching the achiral Cu surfaces to a chiral surface, Cu(3,1,17)^S, as shown in Fig. 4a, we can utilize AIMAP to predict whether the chirality recognition is present for AA adsorption on the chiral Cu surface. The
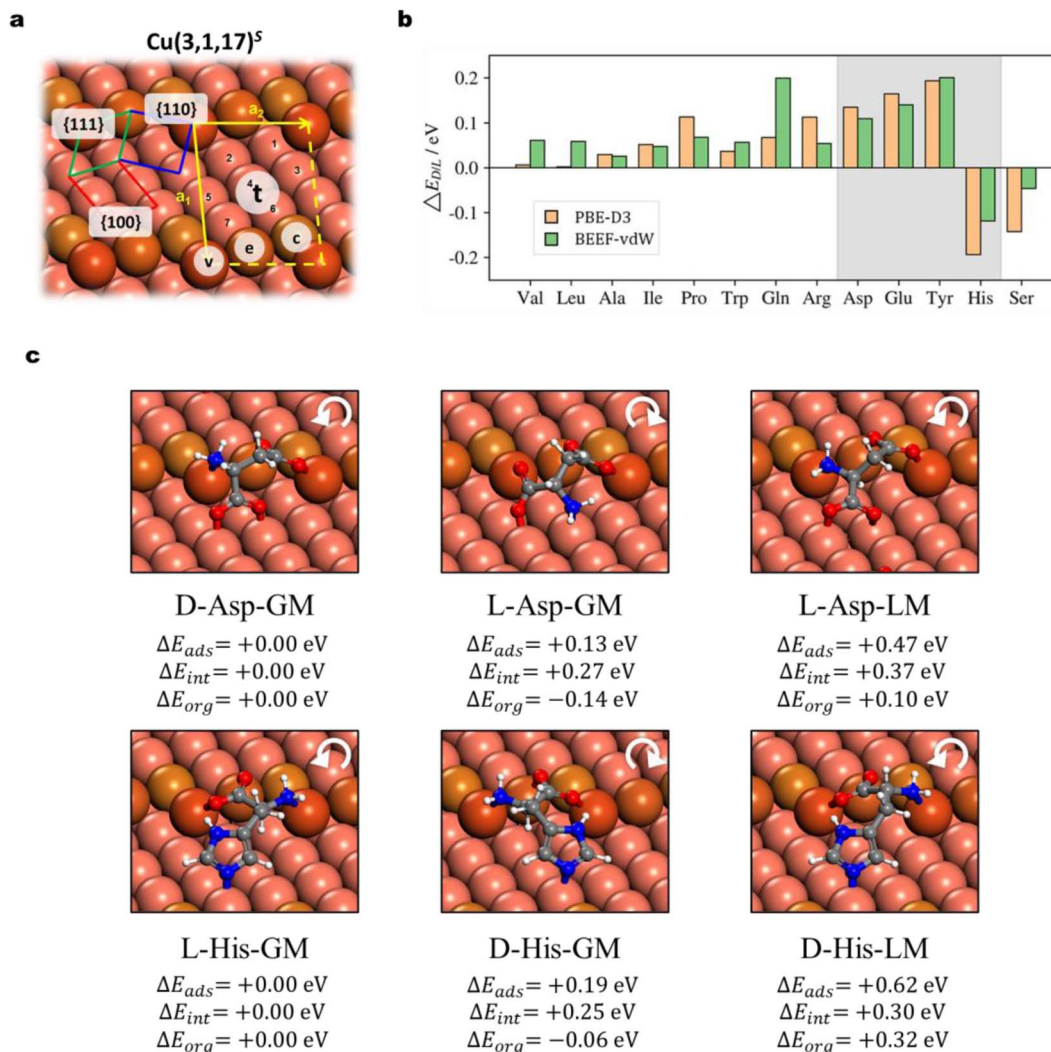
Fig. 4 Enantio-specific adsorption on the Cu(3,1,17)^S surface. (a) The structure of the intrinsic chiral Cu(3,1,17)^S surface. This surface has kinked steps formed by {110} (green) and {111} (blue) microfacets, separated by {100} (red) terraces. This structure is designated as S, with clockwise and counter-clockwise rotations, {111} → {100} → {111}. The yellow arrows denote unit cell vectors. All distinctive adsorption sites are labeled based on the features of copper atoms for adsorption, including the step vertex site v, step edge site e, step corner site c, and terrace sites t_1–t_7. (b) The relative stability ($\Delta E_{L/D}$) of D/L-AAs on Cu(3,1,17)^S adsorption. The green and orange bars represent the $\Delta E_{L/D}$ obtained by PBE-D3 and BEEF-vdW methods, respectively. The four types of AAs exhibiting $|\Delta E_{L/D}| > 0.10$ eV under both of the two functionals are highlighted in grey shadow. (c). Adsorption structures of Asp and His on the Cu(3,1,17)^S surface. Each row contains three structures, including two GM structures of D/L conformers (D/L-GM), and one LM that has the closest molecule–surface connectivity with the most favorable adsorption structure (D-Asp-GM and L-His-GM). Indicated below are the ΔE_{ads}, ΔE_{int} and ΔE_{org} values (see text) of each structure using the most stable adsorption system as the reference. The white cycle arrow highlights the chirality recognition, following the sequence of amino → carboxylate → side chain. Colors in (a) and (c): white balls are H; grey balls are C; blue balls are N; red balls are O; coral balls are Cu (with higher color intensity following t, c, e, and v sites).

Cu(3,1,17)^S surface features kinked steps formed by {110} and {111} microfacets, separated by {100} terraces. The kinked structure is the chiral center, which is designated R and S with clockwise and counter-clockwise rotations in the sequence of {111} → {100} → {110}. On the S surface, D-adsorbates are equivalent to L-adsorbates on the R surface (and *vice versa*). Without losing generality, we focus on the adsorption of D/L-AA on the Cu(3,1,17)^S surface, where their highest deprotonated AA forms are taken as the adsorbates based on the knowledge gleaned from the previous section.

In Fig. 4a, all distinctive sites, including the step vertex site v, step edge site e, step corner site c, and terrace sites t_1–t_7, are labeled. The defective atoms on the step edge (v, e, and c) are primarily considered on arranging the surface precursors, as inspired by the adsorption behavior on the defective Cu(211) surface. A total number of 6420 distinct minima are considered for all 35 types of D/L-AA species, with 346 adsorption structures selected out for further DFT investigations. The adsorption structures are modeled at low-coverage, as the (2 × 1) supercell is utilized for these with relatively small skeleton size (Ala, Val, Pro, Leu, Ile, Ser, Thr, Glu, Gln, Asp, Asn) whereas a (2 × 2)

supercell is applied for the other 6 types (Phe, Trp, Tyr, His, Lys, Arg). All the adsorption structures and the adsorption energy of D and L forms are provided in ESI S7.1 and S7.2† and it is obvious that all D/L-enantiomers adopt distinct local geometry from each other. The relative stability of the most stable D/L-enantiomers is given by:

$$\Delta E_{L/D} = E_{ads}(L) - E_{ads}(D) \quad (3)$$

where a positive $\Delta E_{L/D}$ indicates the preference of D-enantiomers and *vice versa*. Given that the value of $\Delta E_{L/D}$ is typically close to the confidence interval of DFT calculations (*e.g.*, around 0.10 eV), we also applied the BEEF-vdW functional to calculate the value for comparison.[64] Among our calculations, 13 types of chiral AAs show consistent enantiomer preference under both PBE-D3 and BEEF-vdW functionals and these results are depicted in Fig. 4b. The remaining five AAs do not exhibit consistent preference and are not discussed here (see ESI Fig. S8†).

Fig. 4b shows that 11 types of AAs have a preference for the D-enantiomer, including Ala, Val, Leu, Ile, Pro, Asp, Glu, Gln, and Tyr, while 2 types of AAs show a preference for the L-enantiomer, *i.e.* His and Ser. Notably, four types of D/L-enantiomers, *i.e.*, Asp, Glu, Tyr, and His, possess relatively strong ΔE_{ads} (>0.10 eV, shadowed in Fig. 4b) under both the two DFT functionals. From our results, the most chiral recognition system always involves the chemical binding on all three microfacets, {111}, {110}, and {100} (*i.e.*, Asp, Glu, Thr, His; Fig. 4 and ESI Fig. S10, S11†), in which the side-chain must also strongly bind with copper atoms through the N/O-containing groups (*i.e.*, carboxylate, imidazole, and phenolic hydroxide). Molecules with poor binding side chains possess relatively small $\Delta E_{L/D}$ as they only involve chemisorption on {110} and {111} microfacets (*e.g.*, Ala, Leu, Val, see ESI Fig. S9†).

To better understand the chiral recognition, we decompose the adsorption energy E_{ads} into two parts, the one from the structure reorganization energy E_{org} of the individual molecule and the surface in the adsorption system compared to the gas phase molecule and the clean surface, respectively; and the other E_{int} from the interaction of the adsorbed molecule and the surface ($E_{ads} = E_{org} + E_{int}$). By using the most stable adsorption system as the reference (*e.g.*, D-Asp-GM for Asp, Fig. 4c), we thus can obtain the ΔE_{ads} ($=\Delta E_{org} + \Delta E_{int}$) to compare the adsorption energy difference between the most stable form and the other less stable form. For illustration, Fig. 4c shows the adsorption structures of two representative chirality recognition systems, Asp and His, which prefer the D- and L-enantiomer adsorption, respectively. The most stable D- (*e.g.*, D-Asp-GM) and L-forms (*e.g.*, L-Asp-GM) for the two AAs are depicted in this figure, together with the less stable L-form of Asp and D-form of His (L-Asp-LM and D-His-LM), which have the closest adsorbate–surface connectivity with their most stable form (D-Asp-GM and L-His-GM, respectively). The ΔE_{ads}, ΔE_{org} and ΔE_{int} are also indicated for these less stable adsorption structures.

3.2.1 D/L-Asp. For Asp, the D-form GM (D-Asp-GM) is 0.13 eV more stable than the L-form GM (L-Asp-GM). Both of them adopt the μ_5 configuration through the carboxylate-amino skeleton

and the two oxygen atoms in the carboxylate side chain, with the same copper sites involved for adsorption (two v sites, two t sites, and one e site). But their adsorption chirality is different, clockwise in L-Asp-GM or counter-clockwise in D-Asp-GM (Fig. 4c white circle arrow) following the sequence from amino to carboxylate and to the side chain. This could be attributed to the large binding ability of the carboxylate side-chain that wins over the carboxylate-amino skeleton to adsorb at the kinked Cu sites (v, e sites). As a result, in D-Asp-GM, the α-carboxylate group binds on the {100} terrace (t site) and the nitrogen atom binds on the v site, while L-Asp-GM features a reversed connectivity in the two groups, with the α-carboxylate group on the step edge (v, t sites) and amino group on the {100} terrace (t site). This adsorption site exchange results in $\Delta E_{int} = +0.27$ eV for the D-Asp-GM, which can be largely attributed to the poor binding of the carboxylate-amino skeleton, being 0.24 eV less stable in L-Asp-GM (see ESI Fig. S12†). For comparison, if the L-form adopts the same molecule–surface connectivity as D-Asp-GM, as shown in L-Asp-LM, the molecule–surface interaction is even worse ($\Delta E_{int} = +0.37$ eV) at a similar molecular distortion cost ($\Delta E_{org} = +0.10$ eV). This again suggests the obvious chiral recognition between Asp and the Cu(3,1,17)^S surface.

3.2.2 D/L-His. For His, the L-form GM (L-His-GM) is 0.19 eV more stable than the D-form GM (D-His-GM). Both of them utilize the carboxylate-amino skeleton to bind on the step edge (two v sites and one e site), with the side-chain imidazole group binding on the {100} microfacet through the sp^2-nitrogen atom. The enantiomer–surface chiral recognition, as also indicated in Fig. 4c by the white arrow, can also be understood as the result of the bonding competition of the imidazole ring in the side-chain and the carboxylate-amino skeleton to the kinked Cu sites. Obviously, the imidazole group fails to compete with the carboxylate-amino skeleton to bind on the kinked sites since the imidazole ring, being rigid and bulky, cannot form a tri-dentation (two v sites and one e site) geometry. As a result, in L-His-GM, the two oxygen atoms of the carboxylate groups bind on a pair of adjacent v site and e site in the {111} microfacet, along with the nitrogen atoms binding on another v site in the {110} microfacet. In contrast, in D-His-GM, the amino nitrogen atom binds on the v site of the {111} microfacet, with the remaining carboxylate oxygen atoms binding on the {110} microfacet. The binding of the imidazole group on the {100} microfacet utilizes the t_6 site in L-His-GM and the t_7 site in D-His-GM. These differences lead to the more compact geometry of the molecule and the closer contact of D-His-GM with the {100} facet, 0.65 Å smaller for the distance between α-C and t sites. The constrained molecule geometry leads to 0.25 eV (ΔE_{org}) disadvantage in energy, which overwhelms the advantage in the adsorbate–surface interaction ($\Delta E_{int} = 0.06$ eV). Again, we found that the D-form with the same molecule–surface connectivity as L-His-GM is even more unstable ($\Delta E_{ads} = 0.62$ eV), which can be attributed to both the constrained molecule geometry ($\Delta E_{org} = +0.32$ eV) and the poor molecule–surface interaction ($\Delta E_{int} = +0.30$ eV).

Our results highlight four AAs (Asp, Glu, Tye, and His) with a strong tendency of chiral recognition on Cu(3,1,17)^S. They share the same structural feature that the side chain containing

N/O groups also binds strongly with the surface. We note that the D-preference of Asp has been revealed through the TPD experiment: on the Cu(3,1,17)^S surface, Yun *et al.* observed a higher coverage of D-Asp against L-Asp on equilibrium adsorption and estimated a 3.2 ± 0.3 kJ mol^{-1} energetic discrimination through the ratio of D/L-coverage (θ_D/θ_L).[65] On the other hand, experiments also indicate non-enantioselective adsorption for some AAs. For example, when the Cu(3,1,17)$^{R\&S}$ surfaces are exposed to the Ala mixture with different D/L ratios (*i.e.*, 1 : 2, 2 : 1, racemic), the ratio of D- and L-Ala on surface coverages equals the value in the gas phase ($\theta_D/\theta_L = p_D/p_L$).[66] This also agrees with our theoretical prediction of the poor chiral recognition for Ala as reflected by the low $\Delta E_{L/D}$.

One has to keep in mind that a high PES accuracy (*e.g.*, <0.05 eV) is generally required to predict correctly the enantioselectivity, which remains extremely challenging for electronic structure calculations. Our results show that two different DFT functionals could lead to the qualitative discrepancy in the sign of $\Delta E_{L/D}$ in the adsorption of four types of AAs (Thr, Asn, Phe, and Lys). Among them, Phe is known to be non-enantioselective and the D-form of Lys is 2.6 ± 0.3 kJ mol^{-1} more favorable,[10,67] a magnitude below the typically regarded chemical accuracy. Finally, we would like to point out that Ser is an interesting case, where theory predicts a 0.14 eV preference for the L-enantiomer by the PBE-D3 method (0.05 eV by BEEF-vdW), but no enantiomeric excess was observed in experiment for the saturated adsorption of Ser on Cu(3,1,17)^S.[67] While it may still originate from DFT error, we suspect that the chiral recognition of the aggregation forms of adsorbates[17,19,21,68,69] (high coverages with lateral interactions) might be the key reason since only low coverage adsorption is considered in this work.

4 Conclusions

This work develops AIMAP, an AI-based tool, to predict molecule adsorption on surfaces, where SSW-NN global optimization as implemented in LASP software in combination with other cheminformatics tools is utilized to speed up the global potential energy scan of molecular adsorption systems. To demonstrate the efficiency of AIMAP, we create the Cu-HCNO6 adsorption database, including over one million distinct adsorption structures of 9592 adsorbates on three representative low-Miller-index Cu surfaces. This database allows us to obtain comprehensive knowledge on molecule adsorption geometry and the sites with the copper surface, The whole database is openly accessible on the LASP website http://laspmol.lasphub.com/laspmol_surf.asp. We are currently working on to expand the database with more metal/material surfaces.

We apply AIMAP in a challenging problem in surface science, the adsorption and the chiral recognition of AAs on surfaces. Multidentate adsorption structures for 18 types of AAs on three achiral copper surfaces are identified, showing that the deprotonated state is generally preferred in adsorption. For AAs on the intrinsic chiral Cu(3,1,17)^S surface, we predict the D-preference of Asp, Glu, and Tyr, and a L-preference of His. We show that the binding competition effect between the carboxylate-

amino skeleton and the side-chain functional side groups for the kinked Cu sites is critical for achieving enantioselectivity.

Data availability

The data supporting this article have been included as part of the ESI.† The CuCHON and other adsorption databases are available from the website http://laspmol.lasphub.com/laspmol_surf.asp.

Author contributions

Z.-P. L. and G.-L. S. conceived the project and contributed to the design of the calculations and analyses of the data. Z.-X. G. carried out most of the calculations and wrote the draft of the paper. All authors discussed the results and commented on the manuscript.

Conflicts of interest

The authors declare no conflict of interest.

Acknowledgements

Notes and references

1 M. G. Evans and M. Polanyi, *Trans. Faraday Soc.*, 1938, **34**, 11–24.
2 T. Bligaard, J. K. Nørskov, S. Dahl, J. Matthiesen, C. H. Christensen and J. Sehested, *J. Catal.*, 2004, **224**, 206–217.
3 P. A. Mirau, R. R. Naik and P. Gehring, *J. Am. Chem. Soc.*, 2011, **133**, 18243–18248.
4 R. Coppage, J. M. Slocik, M. Sethi, D. B. Pacardo, R. R. Naik and M. R. Knecht, *Angew. Chem., Int. Ed.*, 2010, **22**, 3767–3770.
5 I. A. Banerjee, L. Yu and H. Matsui, *Proc. Natl. Acad. Sci. U. S. A.*, 2003, **100**, 14678–14682.
6 C.-Y. Chiu, Y. Li, L. Ruan, X. Ye, C. B. Murray and Y. Huang, *Nat. Chem.*, 2011, **3**, 393–399.
7 Y. Fang, X. Liu, Z. Liu, L. Han, J. Ai, G. Zhao, O. Terasaki, C. Cui, J. Yang, C. Liu, Z. Zhou, L. Chen and S. Che, *Chem*, 2023, **9**, 460–471.
8 N. Shukla and A. J. Gellman, *Nat. Mater.*, 2020, **19**, 939–945.
9 X. Zhao, *J. Am. Chem. Soc.*, 2000, **122**, 12584–12585.
10 W. Y. Cheong and A. J. Gellman, *J. Phys. Chem. C*, 2011, **115**, 1031–1035.
11 D. S. Sholl, A. Asthagiri and T. D. Power, *J. Phys. Chem. B*, 2001, **105**, 4771–4782.

12 M. M. Antonijevic and M. B. Petrovic, *Int. J. Electrochem. Sci.*, 2008, **3**, 1–28.

13 D. Kumar, N. Jain, V. Jain and B. Rai, *Appl. Surf. Sci.*, 2020, **514**, 145905.

14 Z. Zhang, N. Tian, L. Zhang and L. Wu, *Corros. Sci.*, 2015, **98**, 438–449.

15 A. Kasprzhitskii, G. Lazorenko, T. Nazdracheva, A. Kukharskii, V. Yavna and A. Kochur, *New J. Chem.*, 2021, **45**, 3610–3629.

16 A. Kasprzhitskii and G. Lazorenko, *J. Mol. Liq.*, 2021, **331**, 115782.

17 M. Sacchi, D. J. Wales and S. J. Jenkins, *Phys. Chem. Chem. Phys.*, 2017, **19**, 16600–16605.

18 Y. Wang, S. Yang, M. Fuentes-Cabrera, S. Li and W. Liu, *J. Am. Chem. Soc.*, 2017, **139**, 8167–8173.

19 R. B. Rankin and D. S. Sholl, *J. Chem. Phys.*, 2006, **124**, 074703.

20 H. S. Song and J. W. Han, *J. Phys. Chem. C*, 2015, **119**, 15195–15203.

21 T. Eralp, A. Ievins, A. Shavorskiy, S. J. Jenkins and G. Held, *J. Am. Chem. Soc.*, 2012, **134**, 9615–9621.

22 J. W. Han, J. N. James and D. S. Sholl, *J. Chem. Phys.*, 2011, **135**, 034703.

23 A. A. Peterson, *Top. Catal.*, 2014, **57**, 40–53.

24 R. B. Rankin and D. S. Sholl, *J. Phys. Chem. B*, 2005, **109**, 16764–16773.

25 C. Chen, S. Yang, G. Su, Q. Ji, M. Fuentes-Cabrera, S. Li and W. Liu, *J. Phys. Chem. C*, 2020, **124**, 742–748.

26 K.-S. Yun, S. J. Pai, B. C. Yeo, K.-R. Lee, S.-J. Kim and S. S. Han, *J. Phys. Chem. Lett.*, 2017, **8**, 2812–2818.

27 P. K. Biswas, N. A. Vellore, J. A. Yancey, T. G. Kucukkal, G. Collier, B. R. Brooks, S. J. Stuart and R. A. Latour, *J. Comput. Chem.*, 2012, **33**, 1458–1466.

28 H. Heinz, T.-J. Lin, R. Kishore Mishra and F. S. Emami, *Langmuir*, 2013, **29**, 1754–1765.

29 L. Chanussot, A. Das, S. Goyal, T. Lavril, M. Shuaibi, M. Riviere, K. Tran, J. Heras-Domingo, C. Ho, W. Hu, A. Palizhati, A. Sriram, B. Wood, J. Yoon, D. Parikh, C. L. Zitnick and Z. Ulissi, *ACS Catal.*, 2021, **11**, 6059–6072.

30 A. Kolluru, M. Shuaibi, A. Palizhati, N. Shoghi, A. Das, B. Wood, C. L. Zitnick, J. R. Kitchin and Z. W. Ulissi, *ACS Catal.*, 2022, **12**, 8572–8581.

31 M. Kleber, I. C. Bourg, E. K. Coward, C. M. Hansel, S. C. B. Myneni and N. Nunan, *Nat. Rev. Earth Environ.*, 2021, **2**, 402–421.

32 T. Sedghamiz, M. Bahrami and M. H. Ghatee, *Chem. Phys.*, 2017, **487**, 48–58.

33 S.-H. Park and G. Sposito, *Phys. Rev. Lett.*, 2002, **89**, 085501.

34 L. Guo, S. Kaya, I. B. Obot, X. Zheng and Y. Qiang, *J. Colloid Interface Sci.*, 2017, **506**, 478–485.

35 S. Kr. Saha, A. Dutta, P. Ghosh, D. Sukul and P. Banerjee, *Phys. Chem. Chem. Phys.*, 2015, **17**, 5679–5690.

36 K. Krautgasser, C. Panosetti, D. Palagin, K. Reuter and R. J. Maurer, *J. Chem. Phys.*, 2016, **145**, 084117.

37 S. Kim, J. Chen, T. Cheng, A. Gindulyte, J. He, S. He, Q. Li, B. A. Shoemaker, P. A. Thiessen, B. Yu, L. Zaslavsky, J. Zhang and E. E. Bolton, *Nucleic Acids Res.*, 2023, **51**, D1373–D1380.

38 J. Lan, A. Palizhati, M. Shuaibi, B. M. Wood, B. Wander, A. Das, M. Uyttendaele, C. L. Zitnick and Z. W. Ulissi, *npj Comput. Mater.*, 2023, **9**, 172.

39 H. Jung, L. Sauerland, S. Stocker, K. Reuter and J. T. Margraf, *npj Comput. Mater.*, 2023, **9**, 144.

40 S. Huang, C. Shang, P. Kang, X. Zhang and Z. Liu, *Wiley Interdiscip. Rev.: Comput. Mol. Sci.*, 2019, **9**(6), e1415.

41 C. Shang and Z.-P. Liu, *J. Chem. Theory Comput.*, 2013, **9**, 1838–1845.

42 P.-L. Kang, Z.-X. Yang, C. Shang and Z.-P. Liu, *J. Chem. Theory Comput.*, 2023, **19**, 7972–7981.

43 D. Chen, L. Chen, Q.-C. Zhao, Z.-X. Yang, C. Shang and Z.-P. Liu, *Nat. Catal.*, 2024, 1–10.

44 J.-L. Li, Y.-F. Li and Z.-P. Liu, *JACS Au*, 2023, **3**, 1162–1175.

45 Q.-Y. Liu, C. Shang and Z.-P. Liu, *J. Am. Chem. Soc.*, 2021, **143**, 11109–11120.

46 S. Ma, S.-D. Huang and Z.-P. Liu, *Nat. Catal.*, 2019, **2**, 671–677.

47 P.-L. Kang, C. Shang and Z.-P. Liu, *J. Am. Chem. Soc.*, 2019, **141**, 20525–20536.

48 Y.-F. Shi, P.-L. Kang, C. Shang and Z.-P. Liu, *J. Am. Chem. Soc.*, 2022, **144**, 13401–13414.

49 N. M. O'Boyle, M. Banck, C. A. James, C. Morley, T. Vandermeersch and G. R. Hutchison, *J. Cheminf.*, 2011, **3**, 33.

50 S. Spicher and S. Grimme, *Angew. Chem., Int. Ed.*, 2020, 15665–15673.

51 C. Bannwarth, E. Caldeweyher, S. Ehlert, A. Hansen, P. Pracht, J. Seibert, S. Spicher and S. Grimme, *Wiley Interdiscip. Rev.: Comput. Mol. Sci.*, 2021, **11**(2), e1493.

52 J. R. Boes, O. Mamun, K. Winther and T. Bligaard, *J. Phys. Chem. A*, 2019, **123**, 2281–2285.

53 W. M. Haynes, D. R. Lide and T. J. Bruno, *Handbook of Chemistry and Physics*, CRC Press, Boca Raton, 97th edn, 2016.

54 J. Williams, S. Haq and R. Raval, *Surf. Sci.*, 1996, **368**, 303–309.

55 X. Zhao, Z. Gai, R. G. Zhao, W. S. Yang and T. Sakurai, *Surf. Sci.*, 1999, **424**, L347–L351.

56 S. M. Barlow, K. J. Kitching, S. Haq and N. V. Richardson, *Surf. Sci.*, 1998, **401**, 322–335.

57 M. Nyberg, J. Hasselström, O. Karis, N. Wassdahl, M. Weinelt, A. Nilsson and L. G. M. Pettersson, *J. Chem. Phys.*, 2000, **112**, 5420–5427.

58 N. A. Booth, D. P. Woodruff, O. Schaff, T. Gießel, R. Lindsay, P. Baumgärtel and A. M. Bradshaw, *Surf. Sci.*, 1998, **397**, 258–269.

59 G. Jones, L. B. Jones, F. Thibault-Starzyk, E. A. Seddon, R. Raval, S. J. Jenkins and G. Held, *Surf. Sci.*, 2006, **600**, 1924–1935.

60 T. Eralp, A. Shavorskiy, Z. V. Zheleva, G. Held, N. Kalashnyk, Y. Ning and T. R. Linderoth, *Langmuir*, 2010, **26**, 18841–18851.

61 S. Dutta and A. J. Gellman, *Chirality*, 2020, **32**, 200–214.

62 J.-H. Kang, R. L. Toomes, M. Polcik, M. Kittel, J.-T. Hoeft, V. Efstathiou, D. P. Woodruff and A. M. Bradshaw, *J. Chem. Phys.*, 2003, **118**, 6059–6071.

63 B. S. Mhatre, Super-Enantiospecific Autocatalytic Decomposition of Tartaric Acid and Aspartic Acid on Cu Surfaces, PhD thesis, Carnegie Mellon University, Pittsburgh, PA, 2013.

64 J. Wellendorff, K. T. Lundgaard, A. Møgelhøj, V. Petzold, D. D. Landis, J. K. Nørskov, T. Bligaard and K. W. Jacobsen, *Phys. Rev. B: Condens. Matter Mater. Phys.*, 2012, **85**, 235149.

65 Y. Yun and A. J. Gellman, *Angew. Chem., Int. Ed.*, 2013, **52**, 3394–3397.

66 Y. Yun, D. Wei, D. S. Sholl and A. J. Gellman, *J. Phys. Chem. C*, 2014, **118**, 14957–14966.

67 Y. Yun and A. J. Gellman, *Langmuir*, 2015, **31**, 6055–6063.

68 Y. Yun and A. J. Gellman, *J. Phys. Chem. C*, 2016, **120**, 27285–27295.

69 R. B. Rankin and D. S. Sholl, *Langmuir*, 2006, **22**, 8096–8103.